Environ Fluid Mech (2007) 7:259–270
DOI 10.1007/s10652-007-9022-y

ORIGINAL ARTICLE

Surface waves and roughness in self-aerated supercritical flow

Luke Toombes · Hubert Chanson

Received: 17 December 2006 / Accepted: 1 March 2007 / Published online: 8 May 2007

Abstract In high-velocity open channel flows, free-surface aeration is commonly observed. The effects of surface waves on the air–water flow properties are tested herein. The study simulates the air–water flow past a fixed-location phase-detection probe by introducing random fluctuations of the flow depth. The present model yields results that are close to experimental observations in terms of void fraction, bubble count rate and bubble/droplet chord size distributions. The results show that the surface waves have relatively little impact on the void fraction profiles, but that the bubble count rate profiles and the distributions of bubble and chord sizes are affected by the presence of surface waves.

Keywords Air–water flows · Surface waves · Surface roughness · Interfacial aeration · Bubble count rate · Self-aerated flows

Introduction

Supercritical open channel flows are highly turbulent flows, and some interfacial aeration at the free surface is commonly observed. A typical example is a supercritical flow down a spillway chute (Fig. 1). In the highly aerated flow region where the void fraction C exceeds 0.3, the microscopic two-phase flow structure is complex, and it consists of a wide range of entities including air–water projections, foam, and complicated air–water imbrications (e.g. [1,2]). Killen [3] argued the possibility of surface waves riding over a bubbly flow region. Brocchini and Peregrine [4] discussed the air–water interfacial zone in terms of intermittency. It is acknowledged, however, a lack of understanding of the air–water flow structure and dynamics for void fractions between 0.3 and 0.7 [1,2,5]. Several people, including

L. Toombes
Connell Wagner, 433 Boundary St, Spring Hill 4000, Australia

L. Toombes · H. Chanson (✉)
Division of Civil Engineering, The University of Queensland, Brisbane, QLD 4072, Australia
e-mail: h.chanson@uq.edu.au
URL: http://www.uq.edu.au/~e2hchans/

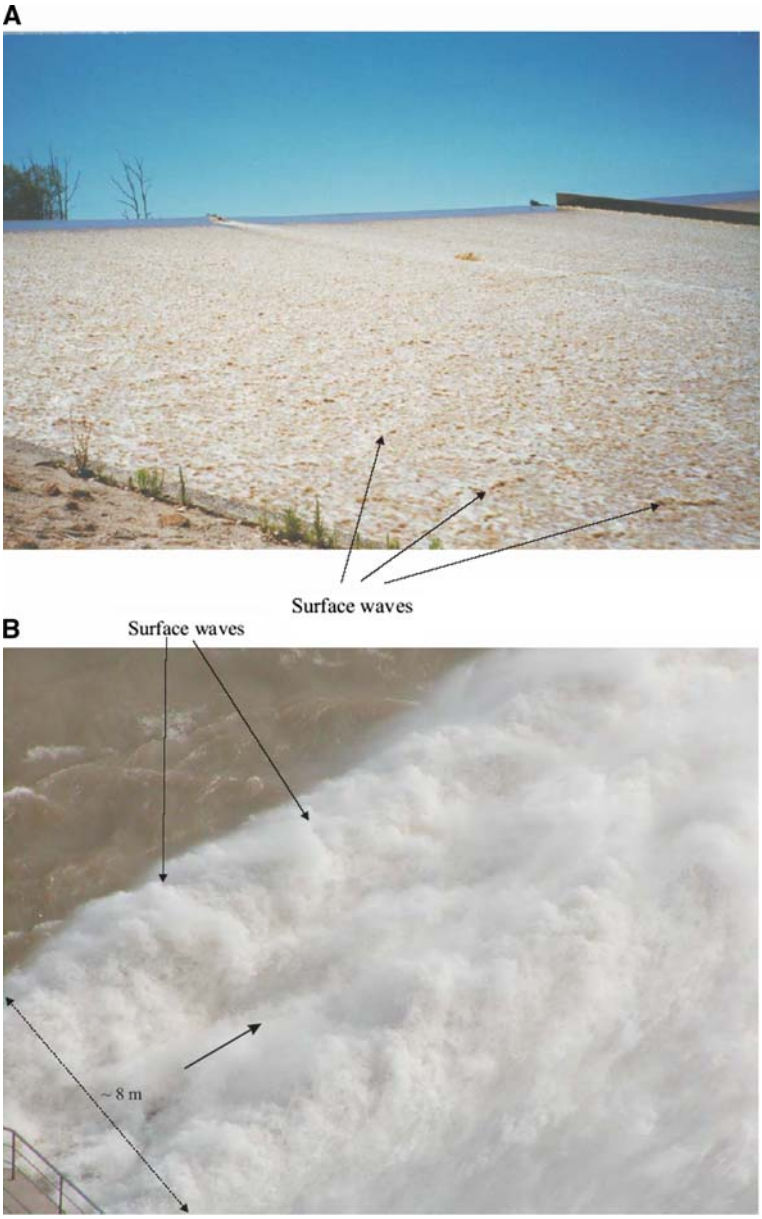

Fig. 1 Self-aerated flows in prototype spillways. (**A**) Chinchilla weir spillway in operation on 8 November 1997. (**B**) Details of bottom outlet jet at the Three Gorges Project (China) on 20 Oct. 2004—$V = 35$ m/s (flow from bottom left to right), jet width: 8 m, shutter speed: 1/1,000 s

the second writer, observed some "wavy" patterns in prototype spillways. For example, in Fig. 1A, the surface wave length was about 1–3 m; in Fig. 1B, interfacial waves with wave lengths of about 4–10 m were seen.

Traditionally, air–water flows were investigated with phase-detection probes that were fixed in space (Fig. 2A). Figure 2A illustrates a typical situation including a typical

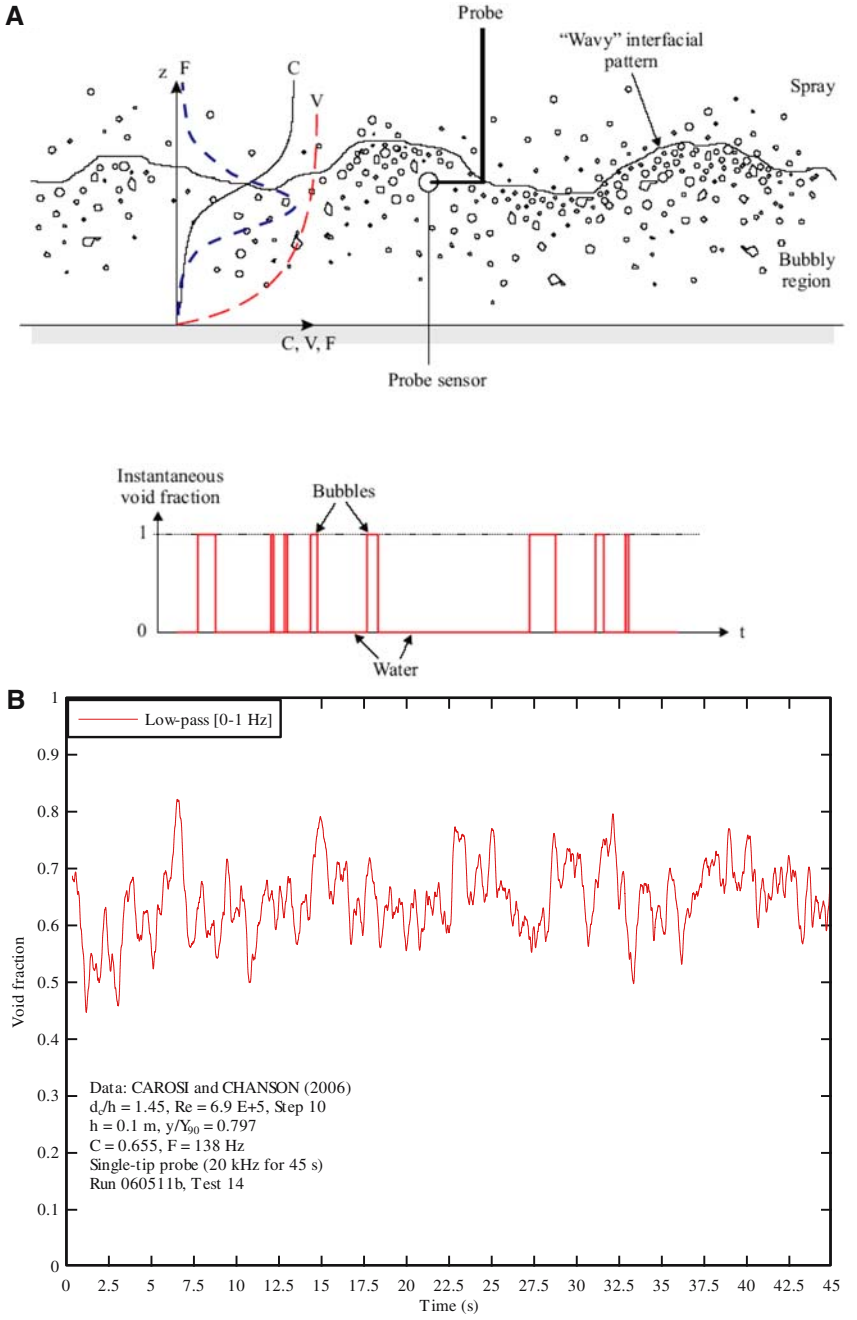

Fig. 2 Air–water structure in a free surface flow. (**A**) Definition sketch. (**B**) Low-pass filtered (0–1 Hz) void fraction data in a stepped channel (Data: Carosi and Chanson [8])—Scan rate: 20 kHz, scan duration: 45 s, $C = 0.66$, $F = 138$ Hz, $y/Y_{90} = 0.80$

instantaneous void fraction signal, where the instantaneous void fraction equals 0 (water) or 1 (air). The signal output from a fixed probe was always fluctuating. Figure 2B presents some low-pass filtered void fraction data for a 45 s scan. The probe signal output was scanned at 20 kHz and the flow conditions are detailed in the figure caption. The data shown in Fig. 2B suggested some fairly substantial oscillations of the void fraction with periods between 2 and 10 s.

It is the aim of this work to provide some new understanding of the air–water flow structure in supercritical open flows. The study examines the effects of surface waves and surface roughness on the air–water flow properties, especially the void fraction and bubble count rate. The basic air–water flow properties of self-aerated flows are presented in the following paragraph. Then a conceptual model of surface waves is proposed, before the results are discussed.

Self-aerated flow properties

In self-aerated supercritical flows, a study of the air–water characteristics involves an investigation of the properties over a complete range of void fractions: i.e., a transition from pure water ($C = 0\%$) to pure air ($C = 100\%$). At low air concentrations (i.e., $C < 30\%$), air-bubbles typically exist as discrete bubbles, or pockets of air, completely surrounded by water. Conversely, at high air concentrations the mixture is mainly discrete water-droplets surrounded by air. For intermediate air concentrations (i.e., $0.3 < C < 0.7$), the air–water structure is complex, and its nature has not been clearly defined.

Experimental studies of self-aerated flows are commonly conducted with phase-detection probes, namely conductivity or optical-fibre probes, fixed in space (e.g. [5,6]). Figure 2 illustrates an example with a typical probe signal output and Table 1 summarises pertinent experimental data sets. The analysis of experimental data shows that the vertical distribution of void fraction follows closely an analytical solution of the advective diffusion equation of air bubbles:

Table 1 Experimental investigations of supercritical open channel flows

References (1)	Slope degrees (2)	q_w m^2/s (3)	Re (4)	Comments (5)
Prototype Chutes Cain [9]	45.0	2.23, 3.16	8.9 E+6 to 1.3 E+7	Aviemore dam spilway (NZ) Concrete chute
Aivazyan [10]	21.8	0.38–1.55	1.5to 5.8 E+6	Erevan dam spillway (Armenia) Rough basalt and cement mortar
	28.1	0.49–1.28	1.9 to 5 E+6	Gizel'don chute (Armenia) Wooden chute
Laboratory studies Straub and Anderson [11]	7.5–75	0.14–0.93	4.7 E+5 to 2 E+6	$W = 0.46$ m
Aivazyan [10]	16.7, 29.7	0.064–0.13	2.3–4.3 E+5	Painted board ($W = 0.25$ m)
Arreguin and Echavez [12]	0	4.4	5.4 E+6	Galvanised tin ($W = 0.2$ m)
Xi [13]	52.5	0.32	1.2 E+6	Timber flume ($W = 0.6$ m)
Chanson [14]	52.3	0.21–0.48	8 E+5 to 2 E+6	Perspex flume ($W = 0.25$ m)
Chanson [15]	4.0	0.142–0.164	5.1 to 5.8 E+5	Painted timber ($W = 0.5$ m)
Toombes [16]	0	0.08–0.136	3.2 to 5.4 E+5	Perspex flume ($W = 0.25$ m)

Notes: Re, Reynolds number defined in terms of the hydraulic diameter; W, channel width

$$C = 1 - \tanh^2\left(K' - \frac{\frac{z}{Z_{90}}}{2\,D'}\right) \tag{1}$$

where z is the distance normal to the invert, and Z_{90} is the characteristic distance where $C = 0.90$ [7]. K' and D' are, respectively, a dimensionless integration constant and the dimensionless diffusivity that are related to the depth-averaged void fraction C_{mean}:

$$C_{\text{mean}} = 2\,D'\left(\tanh\left[0.327 + \frac{1}{2\,D'}\right] - 0.316\right) \tag{2}$$

$$K' = 0.327 + \frac{1}{2\,D'} \tag{3}$$

Equation 1 is compared with some prototype spillway data [9] in Fig. 3A.

The bubble count rate F is defined as the number of bubbles impacting a probe sensor per second. It characterises the flow fragmentation and it is proportional to the air–water specific interface area. Experimental measurements showed that the relationship between bubble frequency and void fraction has a quasi-parabolic shape with the frequency reaching a maximum at about $C = 0.5$, and decreasing to zero as C tends to 0 and 1. However, the relationship is often asymmetrical: i.e., the maximum bubble frequency does not coincide with $C = 0.5$. A predictive model, based upon the characteristics of the streamwise structure of the air–water flow, may be based upon some correction factors that are functions of the local void fraction and flow conditions:

$$\frac{F}{F_{\max}} = \frac{1}{\left(1 + \left(\frac{\lambda_w}{\lambda_a} - 1\right)C\right)\left(1 - b\,(1 - 2\,C)^4\right)}\;\frac{C\,(1 - C)}{\left(\frac{\sqrt{\lambda_w/\lambda_a} - 1}{\lambda_w/\lambda_a - 1}\right)^2} \tag{4}$$

where $F_{\max}$ is the maximum bubble count rate in the cross-section, λ is a micro-length scale such that the probability of a discrete element of that size being air (λ_a) or water (λ_w) is independent of the surrounding segments, λ_w/λ_a is the ratio of the average water micro-length scale to the corresponding air micro-length scale, and b is a constant (Appendix A). Further details on the derivation of Eq. 4 are given in Appendix A. For $\lambda_w/\lambda_a = 1$, Eq. 4 becomes an exact parabola:

$$\frac{F}{F_{\max}} = 4\,C\,(1 - C) \tag{5}$$

Equations 4 and 5 are compared with prototype spillway data in Fig. 3B.

Another reasoning yields a relationship similar to Eq. 5. The bubble count rate F equals half of the number of air–water interfaces. That is, F must be proportional to the rate of change of the instantaneous void fraction: $F \equiv {C_{\text{rms}}}^2$. The probability distribution function of the instantaneous void fraction is bi-modal. A simple derivation shows that its variance ${C_{\text{rms}}}^2$ equals $C(1 - C)$ where the void fraction C is the time-averaged local void fraction:

$$F \equiv {C_{\text{rms}}}^2 = C\,(1 - C) \tag{6}$$

In Eq. 6, the coefficient of proportionality between F and ${C_{\text{rms}}}^2$ is 4 $F_{\max}$ (Eq. 5).

Experimental results showed further that the velocity distribution follows closely a power law:

$$\frac{V}{V_{90}} = \left(\frac{z}{Z_{90}}\right)^{1/N} \tag{7}$$

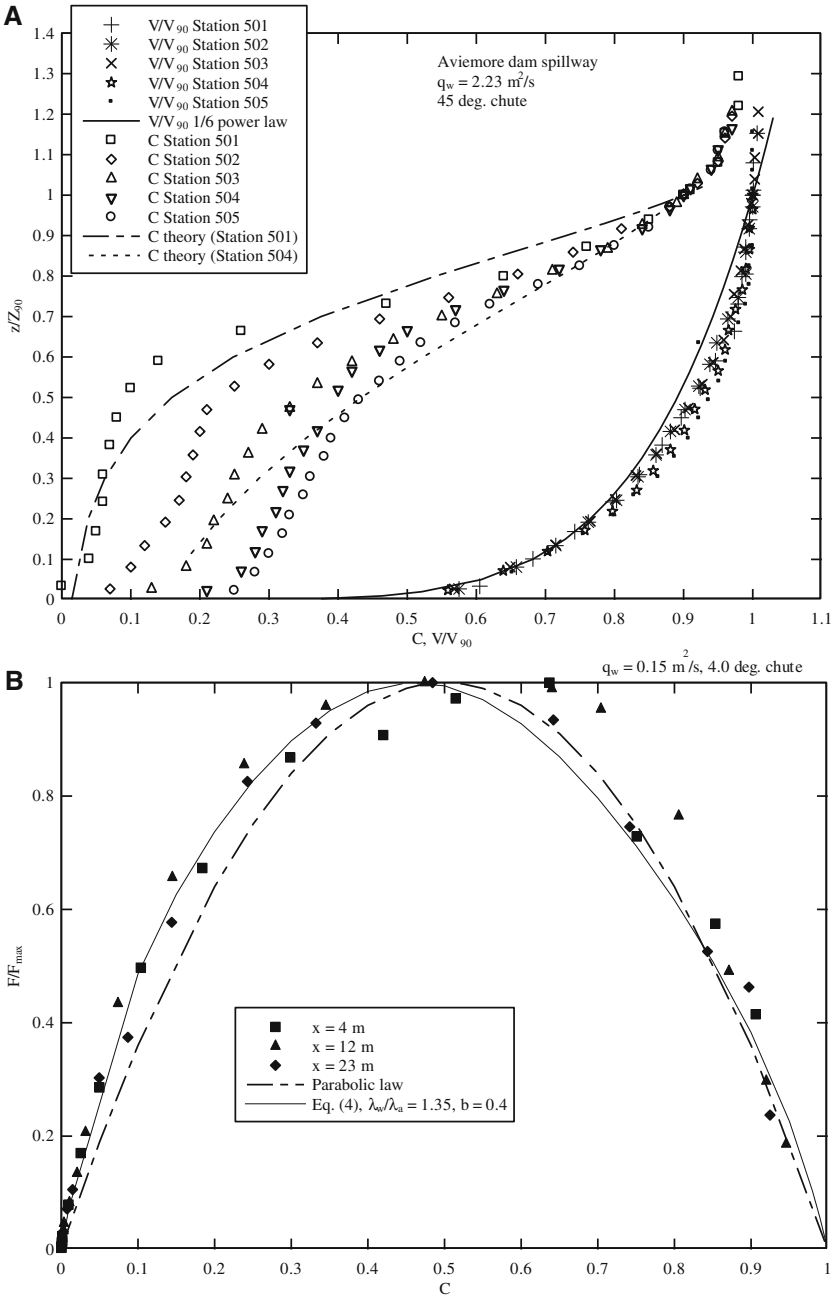

Fig. 3 Air–water flow properties on a smooth-invert chute. (**A**) Dimensionless distributions of void fraction and velocity—Comparison between data [9] and Eqs. 1 and 7. (**B**) Dimensionless relationship between void fraction and bubble count rate—Comparison between data [15] and Eqs. 4 and 5

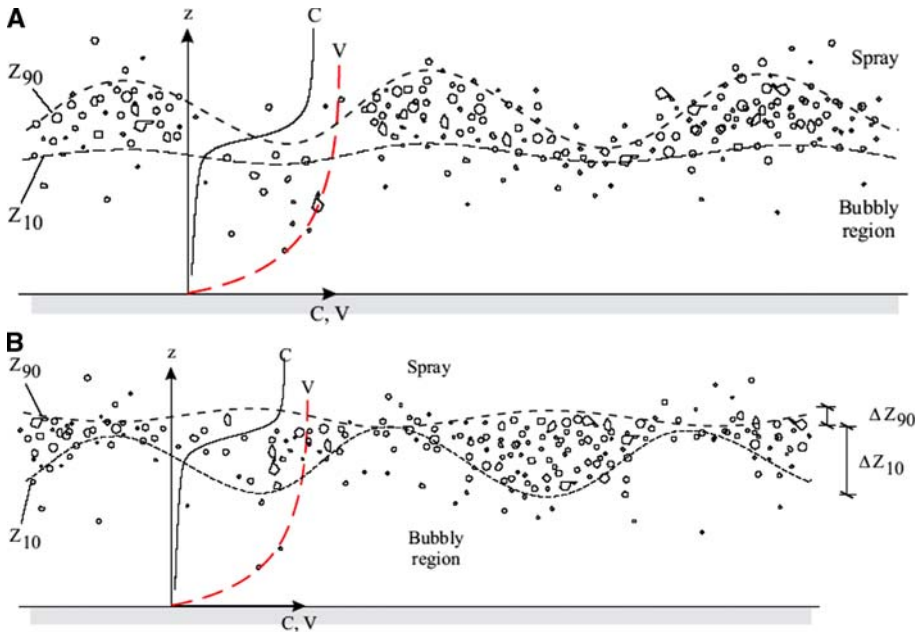

Fig. 4 Unsteady void fraction profiles. (**A**) Surface wave. (**B**) Bubbly flow surge/plug flow situation

where V_{90} is the characteristic air–water velocity at $z = Z_{90}$ and the inverse of the velocity exponent is about $N = 6$ [9,15,17]. Prototype data are presented in Fig. 3A and compared with Eq. 7.

Surface wave modelling

An intrusive phase-detection probe (e.g., conductivity or optical probe) detects the passage of air–water interfaces at a fixed point. Figure 4 illustrates some hypothetical situation with some surface "waves". The effects on the air–water flow properties are investigated herein using a numerical simulation. The numerical model simulates the flow of an air–water mixture past a probe sensor by generating a stream of successive air-bubble and water-droplet chord lengths that would be recorded by a phase-detection intrusive probe. The parameters used to generate the "signal" are then modified in response to some wave form oscillation of the water depth. This model was developed specifically to model a "surface wave" in a supercritical open channel flow down a smooth-invert. Yet other flow situations, such as the cyclic oscillation of the free-falling jet, may result in similar modifications to the air–water flow properties recorded by a fixed probe.

The void fraction profiles (Eq. 1) imply that there is not an absolute air–water free surface. Rather the time-averaged void fraction C increases with distance from the invert in a smooth transition from water to air (Fig. 3A). Any "surface wave" must be considered as a variation of the air concentration profile which is described by two basic parameters: the depth-average air concentration C_{mean} and the elevation Z_{90} where $C = 0.9$. It is assumed that the free surface fluctuations take the form of sinusoidal waveforms, with wave lengths and amplitudes that deviate randomly about a specified mean. The fluctuations of Z_{90} with time are given as:

$$Z_{90} = \widetilde{Z}_{90} + A \sin\left(2\pi \frac{V\ (t - t_0)}{L_w}\right) \tag{8}$$

where t is the time, and A and L_w are the wave amplitude and length, respectively. The wave length and the magnitude of the amplitude of the wave were represented by a Weibull probability distribution, and the deviation about the mean (i.e. $(Z_{90} - \widetilde{Z}_{90})$) were represented by a normal probability distribution [16].

The variations of the velocity distribution with time are deduced from the power law for a varying characteristic depth Z_{90}:

$$\frac{V}{\widetilde{V}_{90}} = \frac{\widetilde{Z}_{90}}{Z_{90}} \left(\frac{z}{Z_{90}}\right)^{1/N} \tag{9}$$

A random sample of air bubble and water droplet chords was generated. The results were then compared with several experimental data sets [9,15,16].

Results

Effect on the void fraction distribution

A systematic investigation was conducted using a wide range of parameters: e.g., a ratio of wave amplitude to depth $A/\widetilde{Z}_{90}$ between 0 and 0.26, a depth-averaged void fraction C_{mean} from 0.18 to 0.22. The results showed that the void fraction profile of the wave-affected flow is a function primarily of the time-averaged void fraction distribution parameters (i.e., $\widetilde{Z}_{90}$ and C_{mean}) and of the relative wave amplitude $A/\widetilde{Z}_{90}$. The wave length, the bubble count rate distribution parameters (F_{max}, λ_w/λ_a, b) and the ratio of average chord to standard deviation of chord were all found to have little influence on the shape of the void fraction distributions.

A comparison of time-averaged void fraction distributions is shown for a range of wave amplitudes in Figure 5. The values of $\widetilde{Z}_{90}$ and C_{mean} are selected to match the experimental observations. The effect of the surface waves was to "stretch" the time-averaged void fraction distribution. The effect was amplified with increased distance z from the invert where the magnitude of the oscillation is greater (amplitude $\propto z/Y_{90}$). Overall, the results showed a somewhat moderate influence (Fig. 5).

Effect on the bubble count rate distribution

The bubble count rate gives an indication of the flux of air bubbles past the fixed probe sensor. The results showed a clear trend implying that the void fraction corresponding to the maximum bubble count rate F_{max} decreased with increasing wave amplitude. This implied that the presence of a depth oscillation played some part in the unsymmetrical shape observed in the bubble count rate data (Figs. 3B, 6). Typical results are presented in Fig. 6 for the same conditions as those of Fig. 5.

The experimental results shown in Figs. 3B, 6 were typical of air–water flow situations with a ratio $\lambda_w/\lambda_a > 1$ (Eq. 4). In some situations, a ratio of $\lambda_w/\lambda_a < 1$ may be observed in the experimental data, which could not be explained using the surface wave form adopted herein. The numerical simulation was possibly too simplified. Physically, a ratio of $\lambda_w/\lambda_a < 1$ may be the result of a surge of bubbles progressing down the channel (i.e. $\Delta Z_{10} > \Delta Z_{90}$) or a bubbly plug flow as sketched in Fig. 4B.

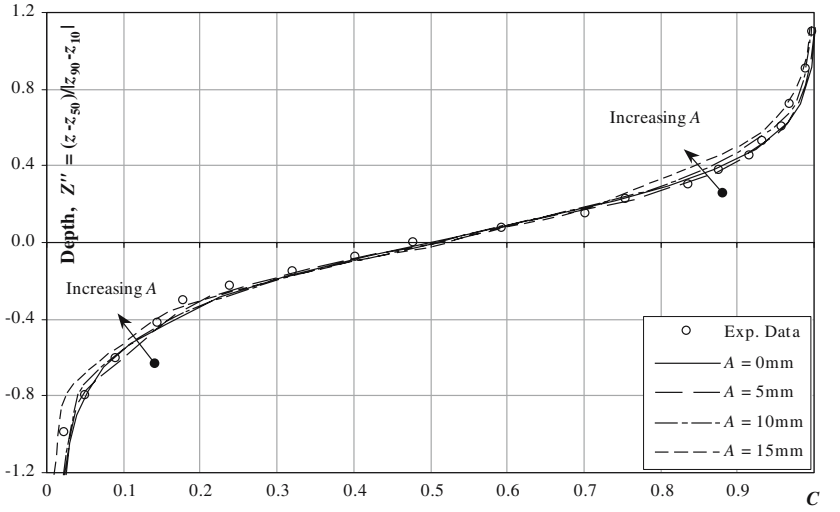

Fig. 5 Effect of the wave amplitude on the void fraction distribution: numerical calculations conducted assuming a ratio of standard deviation to average chord for both air and water of 1.5, and dimensionless wave length $L_w/\tilde{Z}_{90} = 3.5$—Comparison with experimental data: $q_w = 0.105\,m^2/s$, $Z_{90} = 0.0572\,m$, $Z_{10} = 0.031\,m$, $Z_{50} = 0.0464\,m$, $C_{mean} = 0.22$ [16]

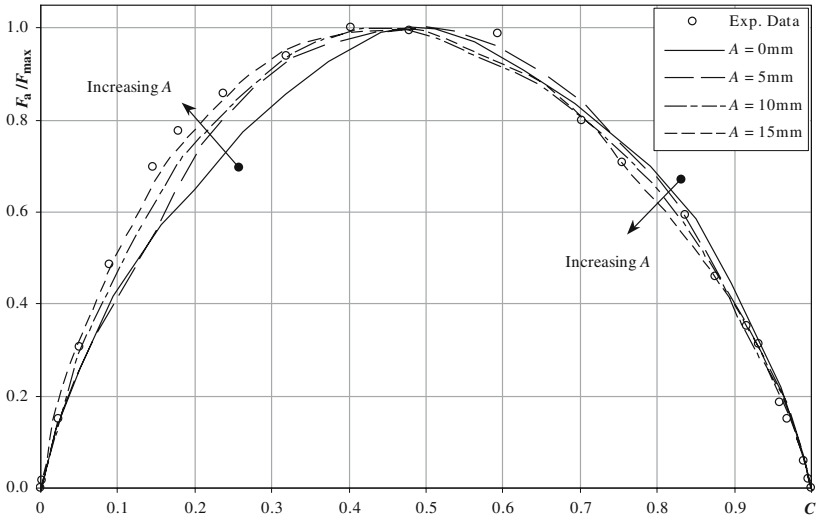

Fig. 6 Modification of the bubble count rate distribution with surface wave amplitude

Effect on the chord size distributions

A wave pattern was initially expected to introduce a number of "large" chord lengths. The results suggested that the chord length distributions were modified significantly by the presence of surface waves. In presence of waves, the percentage of "large" bubble chord in the chord-length distribution became increasingly larger with increasing mean chord length, than in absence of waves. Further the percentage of large chord lengths increased with both

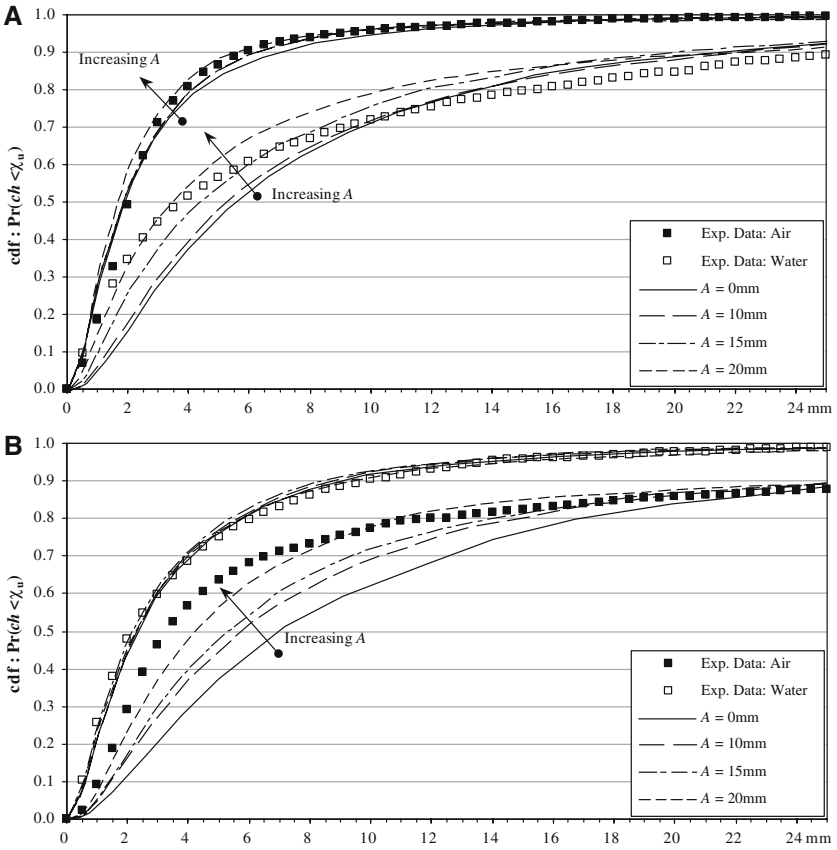

Fig. 7 Modification of chord length distribution with wave amplitude—Comparison with experimental data: $q_w = 0.105\,m^2/s$, $Z_{90} = 0.0572\,m$, $C_{mean} = 0.22$ [16]. (**A**) Cumulative probability distribution functions of air bubble chord—Data at $z = 0.040\,m$, $C = 0.24$, $F = 249\,Hz$, $V = 3.21\,m/s$. (**B**) Cumulative probability distribution functions of water droplet chord—Data at $z = 0.052$, $C = 0.75$, $F = 205\,Hz$, $V = 3.38\,m/s$

wave amplitude and wave length. Figure 7 shows some comparison between the numerical simulation and experimental data. Figure 7A presents some chord cumulative probability distribution functions in the bubbly flow region, while Fig. 7B illustrates some chord data in the spray region. For each graph, the details of the experimental conditions are given in the figure caption.

The chord distribution results produced by the simulation displayed some distinct trends that resembled the behaviour of experimental data. These results would appear to confirm the hypothesis that the experimental data obtained with a fixed probe were influenced by surface waves and roughness oscillations.

Conclusion

The study is focused on the air–water flow structure in supercritical open channel flows, and the effect of surface waves on the void fraction and bubble count rate distributions recorded by a fixed phase-detection probe. Some detailed comparison between the proposed model

of surface waves and experimental data showed a good agreement. Despite its simplifications, the simulation results suggested that surface waves or fluctuations of the flow depth influenced the air–water flow properties. The presence of surface waves had relatively little effect on the void fraction distributions. But the existence of free-surface waves had a significant influence on the distribution of bubble count rate, and on the relationship between bubble count rate and void faction. More the surface waves caused some modification of the chord length distributions, with the distributions containing an increased percentage of large chord-lengths. The level of modification was a function of the amplitude and wave length of the surface waves, as well as of the mean chord length.

Acknowledgments The writers thank Professor C.J. APELT his valuable advice. The first writer acknowledges the financial support of the Australian Research Council and University of Queensland.

Appendix A - Relationship between bubble count rate and void fraction

The bubble count rate is a function of the average bubble chord-length. A simplified model for an air–water mixture flowing past a fixed probe sensor consists of a series of discrete one-dimensional air and water elements [16]. The characteristic sizes of the discrete air and water elements are given by the length scales λ_a and λ_w, respectively, which are functions of the fragmentation of the flow. The probability of any discrete element to be air is the void fraction C assuming that each segment is either air or water. Each air-bubble is bounded by a transition from water to air and air to water. Assuming that $\lambda_a = \lambda_w$ and that the probability of an element being air or water is independent of the state of adjacent elements, the bubble count rate is derived from the probability of consecutive elements being air and water as:

$$F_{\mathrm{a}} = \frac{V}{\lambda_{\mathrm{a}}} \mathrm{C}(1 - \mathrm{C}) \tag{A-1}$$

where V is the air–water velocity [16]. If V and λ_{a} are constant in the cross-section, the maximum bubble count rate $F_{\max}$ occurs for $C = 0.5$ with $F_{\max} = V/(4^*\lambda_a)$ resulting in the parabolic relationship (Eq. A-1).

An improved model may be derived by introducing two correction factors α and β that are functions of the local void fraction and flow conditions:

$$F_{\mathrm{a}} = \frac{V}{\alpha\beta\lambda} C(1 - C) \tag{A-2}$$

where λ is a constant length scale factor such that the probability of a discrete element of that size being air or water is independent of the surrounding segments. The correction factor α accounts for the average size of discrete air elements λ_{a} having a different value to the average size of water elements λ_{w} at any given point. It is derived from a probability analysis:

$$\alpha = 1 + C\left(\frac{\lambda_{\mathrm{w}}}{\lambda_{\mathrm{a}}} - 1\right) \tag{A-3}$$

In Eq. A-2, the correction factor β allows for some variations of the discrete element length scales λ_{a} and λ_{w} with the void fraction:

$$\beta = 1 - b(1 - 2C)^4 \tag{A-4}$$

where the coefficient b is a constant characteristic of the maximum variations of β with $(1 - b) \leq \beta \leq 1$.

After transformation, Eq. A-2 may be rewritten as:

$$\frac{F}{F_{\max}} = \frac{1}{\left(1 + \left(\frac{\lambda_w}{\lambda_a} - 1\right) C\right) \left(1 - b\,(1 - 2\,C)^4\right)} \; \frac{C\,(1 - C)}{\left(\frac{\sqrt{\lambda_w/\lambda_a} - 1}{\lambda_w/\lambda_a - 1}\right)^2} \tag{A-5}$$

Toombes [16] and Gonzalez [17] tested and applied Equation (A-5) with a wide range of experimental data with Reynolds numbers between 8 E+4 and 1 E+6, including nappe flows and skimming flows on stepped spillways, water jets discharging into atmosphere, and impact flows at a drop.

References

1. Wood IR (1991) Air entrainment in free-surface flows. IAHR hydraulic structures design manual no. 4, hydraulic design considerations, Balkema Publ., Rotterdam, The Netherlands, p 149
2. Chanson, H. (1997a) Air bubble entrainment in free-surface turbulent shear flows. Academic Press, London, UK, p 401
3. Killen JM (1968) The surface characteristics of self-aerated flow in steep channels. PhD thesis, University of Minnesota, Minneapolis, USA
4. Brocchini M, Peregrine DH (2001) The dynamics of strong turbulence at free surfaces. Part 2. Free-surface boundary conditions. J Fluid Mech 449: 255–290
5. Chanson H. (2004) Air-water flows in water engineering and hydraulic structures. Basic processes metrology. In: Yazdandoost F, Attari J (eds) Proceedings of the international conference on Hydraulics of dams and river structures. Tehran, Iran, Keynote lecture, Balkema Publ., The Netherlands, pp 3–16
6. Chang KA, Lim HJ, Su CB (2003) Fiber optic reflectometer for velocity and fraction ratio measurements in multiphase flows. Rev Scientific Inst 74(7):3559–3565. Discussion: (2004), 75(1):284–286
7. Chanson H (1995) Air bubble diffusion in supercritical open channel flow. In: Bilger RW (ed) Proceedings of the 12th Australasian fluid mechanics conference AFMC, vol. 2. Sydney, Australia, pp 707–710
8. Carosi G, Chanson H (2006) Air-water time and length scales in skimming flows on a stepped spillway. Application to the spray characterisation. Report No. CH59/06, Div. of Civil Engineering, The University of Queensland, Brisbane, Australia, p 142
9. Cain P (1978) Measurements within self-aerated flow on a large spillway. PhD thesis, Ref. 78–18, Dept. of Civil Engrg., Univ. of Canterbury, Christchurch, New Zealand
10. Aivazyan OM (1986) Stabilized aeration on chutes. Gidrotekhnicheskoe Stroitel'stvo, No. 12, pp. 33–40 (in Russian). (Translated in Hydrotechnical Construction, 1987, Plenum Publ., pp 713–722)
11. Straub LG, Anderson AG (1958) Experiments on self-aerated flow in open channels. J Hyd Div Proc. ASCE, 84(HY7), 1890-1–1890-35, paper 1890
12. Arreguin F, Echavez G (1986) Natural air entrainment in high velocity flows. In: Proceedings of the conference on advancements in aerodynamics, fluid mechanics and hydraulics. ASCE, Minneapolis, USA, pp 186–192
13. Xi R (1988) Characteristics of self-aerated flow on steep chutes. In: Proceedings of the international symposium on hydraulics for high dams. IAHR, Beijing, China, pp 68–75
14. Chanson H (1988) A study of air entrainment and aeration devices on a spillway model. PhD thesis, Ref. 88–8, Dept. of Civil Engrg., University of Canterbury, New Zealand
15. Chanson H. (1997) Air bubble entrainment in open channels. Flow structure and bubble size distributions. Intl J Multiphase Flow 23(1): 193–203
16. Toombes L (2002) Experimental study of air-water flow properties on low-gradient stepped cascades. PhD thesis, Dept of Civil Engineering, The University of Queensland
17. Gonzalez CA (2005) An experimental study of free-surface aeration on embankment stepped chutes. PhD thesis, Department of Civil Engineering, The University of Queensland, Brisbane, Australia, p 240